# Seasonal cycle of idealized polar clouds: large eddy simulations driven by a GCM

**Xiyue Zhang[1], Tapio Schneider[2,3], Zhaoyi Shen[2], Kyle G. Pressel[4], and Ian Eisenman[5]**

[1]National Center for Atmospheric Research, Boulder, Colorado, USA
[2]California Institute of Technology, Pasadena, California, USA
[3]Jet Propulsion Laboratory, California Institute of Technology, Pasadena, California, USA
[4]Pacific Northwest National Labratory, Richland, Washington, USA
[5]Scripps Institution of Oceanography, University of California, San Diego, California, USA

**Key Points:**

- LES driven by time-varying large-scale forcing from an idealized GCM is used to simulate the seasonal cycle of Arctic clouds
- Simulated low-level cloud liquid is maximal in late summer to early autumn, and minimal in winter, consistent with observations
- Large-scale advection provides the main moisture source for cloud liquid and shapes its seasonal cycle

Corresponding author: X. Zhang, `sallyz@ucar.edu`

## Abstract

The uncertainty in polar cloud feedbacks calls for process understanding of the cloud response to climate warming. As an initial step, we investigate the seasonal cycle of polar clouds in the current climate by adopting a novel modeling framework using large eddy simulations (LES), which explicitly resolve cloud dynamics. Resolved horizontal and vertical advection of heat and moisture from an idealized GCM are prescribed as forcing in the LES. The LES are also forced with prescribed sea ice thickness, but surface temperature, atmospheric temperature, and moisture evolve freely without nudging. A semigray radiative transfer scheme, without water vapor or cloud feedbacks, allows the GCM and LES to achieve closed energy budgets more easily than would be possible with more complex schemes; this allows the mean states in the two models to be consistently compared, without the added complications from interaction with more comprehensive radiation. We show that the LES closely follow the GCM seasonal cycle, and the seasonal cycle of low clouds in the LES resembles observations: maximum cloud liquid occurs in late summer and early autumn, and winter clouds are dominated by ice in the upper troposphere. Large-scale advection of moisture provides the main source of water vapor for the liquid clouds in summer, while a temperature advection peak in winter makes the atmosphere relatively dry and reduces cloud condensate. The framework we develop and employ can be used broadly for studying cloud processes and the response of polar clouds to climate warming.



## Plain Language Summary

The polar regions are changing rapidly. Clouds and their feedbacks remain uncertain due to small-scale unresolved processes in climate models, which contributes to uncertainties in polar climate projection. In order to understand the mechanisms that control polar clouds, we focus on their seasonal cycle in the current climate. We adopt an idealized framework for driving high-resolution simulations by a global climate model. With minimal components represented, we find similar features between the simulated and observed polar clouds. In particular, liquid clouds reach maximum in summer, which coincides with the summer peak in moisture advection from lower latitudes. Therefore, projection of polar clouds will depend on future changes in heat and moisture advection. This framework will allow us to study the response of polar clouds to climate warming.

## 1 Introduction

As the Arctic warms and sea ice cover declines, it is pressing to reduce the uncertainties associated with polar climate change. One of the processes that contributes to Arctic climate change is the cloud radiative feedback (Holland & Bitz, 2003; Vavrus, 2004; Graversen & Wang, 2009). Clouds, depending on their amount, phase composition (liquid and/or ice), and altitude have different radiative effects. Cloud feedbacks in polar regions differ from their frequently studied low-latitude counterparts because polar regions have little to no incoming shortwave radiation in winter, they generally have a high surface albedo from ice cover, and even low clouds in polar regions are often mixed-phase clouds. As a result, the net cloud radiative effect at the surface is positive. i.e., clouds warm the surface because their longwave radiative effect dominates, unlike in low latitudes, where their predominant effect is a cooling of the surface (Shupe & Intrieri, 2004). How this cloud radiative effect changes with climate, and thus feeds back onto climate change, importantly influences the trajectory of Arctic climate change, including the Arctic amplification of climate change (Pithan & Mauritsen, 2014; Kay et al., 2016).

The polar regions are characterized by large insolation variations and hence display a robust seasonal cycle. During the polar night, convergence of advective heat fluxes and surface turbulent heat fluxes become the dominant energy sources for the polar atmosphere. By contrast, insolation is a dominant factor during the polar day. The magnitude of Arctic amplification in response to increased greenhouse gas concentrations also displays marked seasonality. Reanalysis and climate models show the largest surface warming in winter (Serreze et al., 2009; Screen et al., 2012), when shortwave feedbacks, for example, from ice or clouds are weak or absent. Models suggest that a positive longwave feedback from clouds contributes to the maximum winter warming (Bintanja & van der Linden, 2013; Laîné et al., 2016; Yoshimori et al., 2014).

Early studies of Arctic clouds were often limited by the scarcity of observations. However, they have laid the groundwork for characterizing Arctic clouds and their seasonal cycle. For instance, Beesley and Moritz (1999) attempted to explain the seasonal variability of Arctic low clouds using a single-column model. In the model, large-scale forcing based on reanalysis for summer and winter produced a cloudy summer and a clear winter boundary layer (BL), which is consistent with the observed seasonal cycle of Arctic clouds. They also found that artificially shutting off surface evaporation in summer does not eliminate low clouds. This suggests an important role for large-scale forcing in providing moisture and shaping the seasonal cycle of Arctic clouds. It is also essential to have the correct temperature dependency of cloud liquid and ice partitioning, as cloud ice crystals have a shorter residence time than liquid droplets.

Advances in satellite observations over the past decade have provided unprecedented 3D coverage of clouds in polar regions. It is now known that liquid clouds persist throughout the year over the Arctic Ocean, and the low-level liquid-containing cloud fraction is highest in summer and autumn. Ice-dominated clouds, on the other hand, show maximum cloud fraction in the winter upper troposphere (Cesana et al., 2012). Consistently, liquid water path reaches its maximum in August–September and minimum in winter (Lenaerts et al., 2017). However, it remains challenging for GCMs to correctly simulate the present-day seasonal cycle of clouds in the Arctic (Karlsson & Svensson, 2013; Taylor et al., 2019; Kretzschmar et al., 2019; Lenaerts et al., 2017). Recently, Baek et al. (2019) have shown that improved representation of atmospheric heat transport in a GCM alleviates Arctic cloud biases in simulations.

Most studies on polar cloud feedbacks have used GCMs. However, because GCMs rely on cloud and turbulence parameterizations that are often tuned to observations in low latitudes (Brient et al., 2016), the reliability of inferences about polar cloud feedbacks from GCMs is questionable. Here we adopt a complementary approach that uses high-resolution large eddy simulations (LES) to explicitly resolve clouds and turbulence in the polar troposphere. Although LES have been frequently used to study the Arctic boundary layer (Klein et al., 2009; Morrison et al., 2011; Ovchinnikov et al., 2014; Savre et al., 2015), they have been rarely used to simulate the entire Arctic troposphere. The challenge is that LES alone cannot support large-scale circulations because of their limited domain size. We use output from a GCM to provide the large-scale forcing necessary to drive LES. The idea is similar to using GCM output or reanalysis to drive a single-column model (e.g., Dal Gesso & Neggers, 2018), but without relying on cloud parameterizations.

As a first step, we choose an idealized approach that only captures essential processes, including large-scale circulations, a closed surface energy budget, sea ice, and mixed-phase microphysics. Following Shen et al. (2020), we use a GCM with simple radiation and convection schemes but without clouds, to provide horizontal and vertical advection

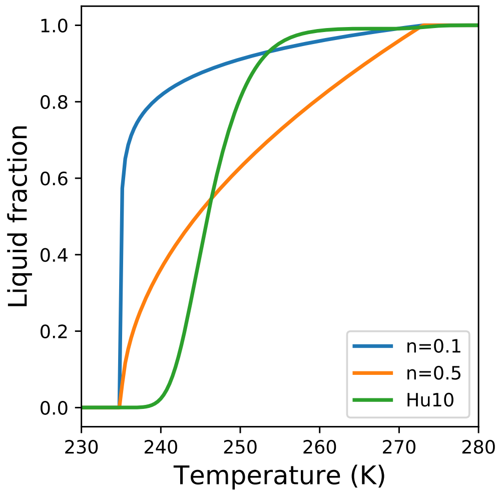


**Figure 1.** Liquid fraction $\lambda(T)$ as a function of temperature $T$ used in one-moment bulk microphysics scheme.

of heat and moisture resolved by the GCM as forcing terms in the LES. Therefore, we can treat each LES as an idealized single GCM column, with turbulent fluxes resolved rather than being parameterized as in the GCM. The simplification in radiation allows the two models to achieve closed energy budgets easily so that they have energetically consistent, though not necessarily realistic, mean state climates. The LES can also provide training data for developing and refining GCM parameterizations (Schneider et al., 2017; Shen et al., 2020).

We address the following questions: Can we reproduce the obseved seasonal cycle of Arctic clouds with our approach? How is the seasonal cycle influenced by large-scale forcing and surface fluxes? In what follows we describe the modeling setup (section 2), followed by results (section 3), discussion (section 4), and conclusions (section 5).

## 2 Model Setup

### 2.1 GCM

We use an idealized moist GCM to simulate large-scale dynamics of an Earth-like atmosphere (Frierson et al., 2006, 2007; O'Gorman & Schneider, 2008). The GCM solves the hydrostatic primitive equation with T42 spectral resolution in the horizontal and 32 unevenly spaced vertical sigma levels. The lower boundary of the GCM is a 5-m thick mixed-layer ocean, and the surface energy budget is closed so that evaporation changes are constrained energetically by changes in other surface energy fluxes. Clouds are not represented in the GCM. Any grid-scale supersaturation is removed immediately to precipitation, and there is no reevaporation of condensate. The GCM uses a gray radiation scheme with prescribed longwave optical thickness. The longwave optical thickness does not vary with water vapor content of the atmosphere, likewise for the shortwave radiation. Therefore, the GCM does not capture water vapor nor cloud feedbacks. The default surface albedo in the aquaplanet configuration is 0.38, but in our case, it also depends on the presence of sea ice. We set the surface albedo to 0.3 for open water, and to 0.5 for sea ice. The surface roughness length is set to $5 \times 10^{-3}$ m for momentum, and to $1 \times 10^{-3}$ m for scalars.

One modification of the GCM specific to the current study is the saturation vapor pressure calculation. In order to obtain consistent thermodynamics, especially at low temperatures, we implemented a look-up table in the GCM to get saturation vapor pressure and its temperature derivatives, instead of using the default formulation in O'Gorman and Schneider (2008). The look-up table is obtained by integrating the Clausius-Clapeyron equation with specific latent heats that depend on temperature (see Equation (1) below). At GCM runtime, the values are determined by linearly interpolating the closest look-up table values. This treatment of saturation vapor pressure is consistent with the LES used in this study (Pressel et al., 2015).

We run the GCM with an obliquity of 23.5°, zero orbital eccentricity, and a seasonal cycle that has a period of 200 days per year. The seasonal cycle is shortened in order to reduce the computational cost of the LES simulations. We refer to the four seasons as the corresponding 50-day averages (e.g., spring is the first 50 days, summer is day 51–100, etc.). We set the longwave optical thicknesses at the equator to $\tau_e = 7.2$ and at the pole to $\tau_p = 1.8$. We run the GCM for 11 years into an approximate statistical equilibrium and use the last year to provide forcing for the LES.

### 2.2 LES

We work with the Python Cloud Large Eddy Simulation code (PyCLES) (Pressel et al., 2015). The model uses an anelastic framework, and it ensures closed total water specific humidity $q_t$ and specific entropy $s$ budgets. PyCLES has been used successfully to simulate subtropical marine BL clouds (Tan et al., 2016, 2017; Pressel et al., 2017; Schneider et al., 2019) and deep convective clouds (Shen et al., 2020).

We use a one-moment mixed-phase microphysics scheme that follows Kaul et al. (2015) and solves prognostic equations for snow and rain water specific humidity separately. Cloud condensates are diagnosed through a saturation adjustment procedure from $q_t$. To partition the total condensate (saturation excess) between liquid and ice, we use a phase partition function that depends on temperature $T$ alone

$$\lambda(T) = \begin{cases} 0 & \text{for} \quad T < T_{\text{cold}}, \\ \left( \dfrac{T - T_{\text{cold}}}{T_{\text{warm}} - T_{\text{cold}}} \right)^n & \text{for} \quad T_{\text{cold}} \leq T \leq T_{\text{warm}}, \\ 1 & \text{for} \quad T_{\text{warm}} < T, \end{cases} \tag{1}$$

where $T_{\text{warm}} = 273$ K and $T_{\text{cold}} = 235$ K are the threshold temperatures for homogeneous melting and freezing (Kaul et al., 2015). The exponent $n$ in the liquid fraction $\lambda$ is taken to be 0.5 (instead of 0.1, a typically used value for Arctic stratocumulus, see Kaul et al. (2015)). The corresponding liquid fraction is shown in Figure 1. Also plotted for comparison is the observationally-derived curve from Hu et al. (2010). Using the latter does not change the simulated seasonal cycle of clouds qualitatively, as will be discussed in section 4.3.

Because the simulations are not limited to Arctic boundary layer clouds, we modified several processes in the microphysics scheme to be applicable to tropospheric clouds. The slope parameter of the particle slope distribution function (PSDF) for snow uses the default formulation in Grabowski (1998) instead of the empirical expression in Morrison et al. (2011) (see also Appendix A in Kaul et al. (2015)). The intercept parameter of the snow PSDF follows the expression in Sekhon and Srivastava (1970).

The LES uses the same gray radiation scheme as the GCM. Because the LES reference pressure can differ substantially from the GCM pressure at the same altitude, we use the GCM pressure and air density to calculate the radiative tendency in the LES. All LES simulations were conducted with a horizontal resolution of 400 m and a vertical resolution that varies from 74 m near the surface to 420 m at the domain top. The three-dimensional LES domain is 25.6 km wide and 18 km high. A sponge layer of 6 km at the top of the domain is implemented to damp the velocity and scalar fluctuations toward the domain-mean values. Simulated clouds below 10 km are insensitive to the sponge layer depth. Therefore, we focus on the representation of the bottom 10 km of the model domain. Like the idealized GCM, the lower boundary of LES is a 5-m thick mixed-layer ocean with closed surface energy budget.

### 2.3 Sea Ice Model

We implemented a thermodynamic sea ice model similar to the Semtner (1976) “zero layer” model. This model was initially developed for a GCM, but we now have implemented in the LES too; however, we prescribe ice thickness in the LES using the GCM output (see Section 2.5). This treatment approximates the specific heat of the ice to be negligible, which implies that the temperature profile within the sea ice remains linear. The present model differs from Semtner (1976) in that for simplicity the freshwater value for the freezing point, $T_{\mathrm{m}} = 273.16$ K, is used at the surface and base of the ice, and a constant latent heat of fusion of ice of $L_{\mathrm{i}} = 3.0\times10^{8}$ J m$^{-3}$ is adopted. Sea ice grows at the base in winter, and ablation occurs at both the surface and the base in summer. There is no surface snow layer and no horizontal sea ice motion.

Where the surface is ice covered ($h_{\mathrm{i}} > 0$), the sea ice thickness evolves according to

$$L_{\mathrm{i}}\frac{dh_{\mathrm{i}}}{dt} = F_{\mathrm{atm}} - F_{\mathrm{base}}. \tag{2}$$

Here the flux exchange between surface and atmosphere $F_{\mathrm{atm}}$ includes radiation and turbulent sensible and latent heat fluxes ($F_{\mathrm{rad}}$, $F_{\mathrm{SH}}$, and $F_{\mathrm{LH}}$, respectively), defined to be positive upward,

$$F_{\mathrm{atm}} = F_{\mathrm{rad}} + F_{\mathrm{SH}} + F_{\mathrm{LH}}. \tag{3}$$

The basal heat flux $F_{\mathrm{base}}$ from the ocean mixed layer into the ice is taken to depend linearly on the temperature gradient between the mixed layer (at $T_{\mathrm{ml}}$) and the ice base (at the melting temperature $T_{\mathrm{m}}$),

$$F_{\mathrm{base}} = F_0(T_{\mathrm{ml}} - T_{\mathrm{m}}),$$

using the coefficient $F_0 = 120$ W m$^{-2}$ K$^{-1}$ as in Eisenman (2007). The surface temperature of the ice $T_{\mathrm{s}}$ is determined implicitly by a balance between the surface flux $F_{\mathrm{atm}}$ (which is a function of $T_{\mathrm{s}}$) and the conductive heat flux through ice,

$$F_{\mathrm{atm}} = k_{\mathrm{i}}\frac{T_{\mathrm{m}} - T_{\mathrm{s}}}{h_{\mathrm{i}}},$$

except where this gives $T_{\mathrm{s}} > T_{\mathrm{m}}$, in which case instead we set

$$T_{\mathrm{s}} = T_{\mathrm{m}},$$

representing surface melt (Eisenman & Wettlaufer, 2009).

The ocean mixed-layer temperature $T_{\mathrm{ml}}$ is determined by

$$\rho_{\mathrm{w}} c_{\mathrm{w}} h_{\mathrm{ml}} \frac{dT_{\mathrm{ml}}}{dt} = -F_{\mathrm{atm}} \tag{4}$$

under ice-free conditions and

$$\rho_{\mathrm{w}} c_{\mathrm{w}} h_{\mathrm{ml}} \frac{dT_{\mathrm{ml}}}{dt} = -F_{\mathrm{base}} \tag{5}$$

where ice is present. Here $\rho_{\mathrm{w}}$ is the density of water, $c_{\mathrm{w}}$ is the specific heat of water, and $h_{\mathrm{ml}}$ is the constant ocean mixed-layer thickness. The representations of the surface fluxes ($F_{\mathrm{rad}}$, $F_{\mathrm{SH}}$, and $F_{\mathrm{LH}}$) do not explicitly depend on whether the surface is ice-covered or ice-free, although they do depend on the surface temperature.

The transition from ice-free to ice-covered conditions happens when $T_{\mathrm{ml}}$ cools below $T_{\mathrm{m}}$ during a GCM time step, in which case frazil ice growth is represented by setting $T_{\mathrm{ml}} = T_{\mathrm{m}}$ and assigning a positive value to $h_{\mathrm{i}}$ equal to this change in $T_{\mathrm{ml}}$ scaled by $L_{\mathrm{i}}$. Similarly, a transition from ice-covered to ice-free conditions occurs when $h_{\mathrm{i}}$ reaches zero, at which point any additional net energy flux warms $T_{\mathrm{ml}}$.

Note that because there is no lateral ocean energy flux ("$Q$ flux") in the present setup, $T_{\mathrm{ml}}$ remains at $T_{\mathrm{m}}$ where ice is present, causing $F_{\mathrm{base}} = 0$.

### 2.4 Large-Scale Forcing

In order to include large-scale dynamics in the limited-domain of LES, we use time-varying large-scale fluxes simulated by the GCM. The details of the forcing framework are described in Shen et al. (2020). In summary, we use LES to simulate a single grid column of a GCM, but with processes that are parameterized in the GCM (e.g., convection, condensation, and boundary layer turbulence) resolved in the LES. The forcing terms include horizontal and vertical advection of temperature and specific humidity, as well as temperature tendencies due to numerical damping and spectral filtering in the GCM.

A major distinction between our forcing framework and that of Shen et al. (2020) is the time-varying forcing. Instead of using the long-time mean tendencies, we use the instantaneous tendencies from the GCM, updated every 6 hours. Therefore, the horizontal advective $q_t$ source term $S_{\mathrm{hadv}}$ becomes

$$S_{\mathrm{hadv}} = -\tilde{u}\partial_x \tilde{q}_t - \tilde{v}\partial_y \tilde{q}_t, \tag{6}$$

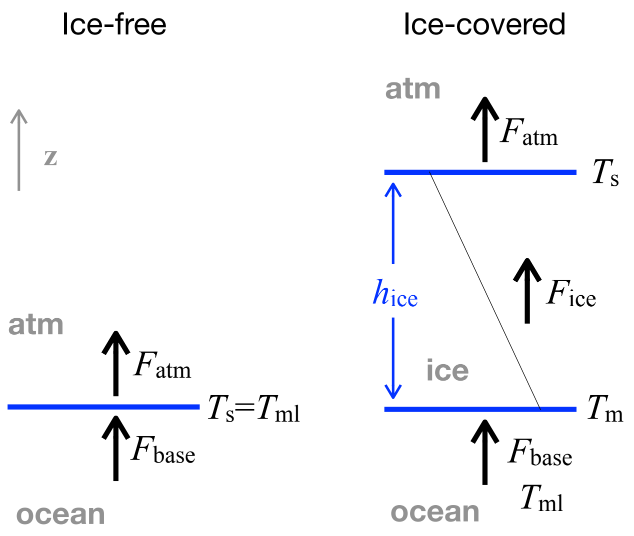


**Figure 2.** Schematics of the surface boundary conditions. In the GCM, the sea ice specific heat is taken to be zero, so that the temperature profile within the ice is linear.

and the vertical advective $q_t$ source term $S_{\mathrm{vadv}}$ becomes

$$S_{\mathrm{vadv}} = -\tilde{w}\partial_z q_t. \tag{7}$$

Tildes $\tilde{(\cdot)}$ denote variables resolved on the GCM grid.

Like for the specific humidity, the horizontal advective temperature tendency $J_{\mathrm{hadv}}$ is taken directly from the GCM,

$$J_{\mathrm{hadv}} = -\tilde{u}\partial_x \tilde{T} - \tilde{v}\partial_y \tilde{T}, \tag{8}$$

and the vertical advective temperature tendency $J_{\mathrm{vadv}}$ becomes

$$J_{\mathrm{vadv}} = -\tilde{w}\partial_z T - \tilde{w}\frac{g}{c_p}, \tag{9}$$

where $g$ is the gravitational acceleration, and $c_p$ is the specific heat of dry air. The source terms (6) and (7) are included in the prognostic equation for $q_t$, and the source terms (6)–(9) are included in the prognostic equation for $s$ (Shen et al., 2020).

For horizontal momentum forcing ($u$ and $v$), we impose the GCM-resolved horizontal momentum tendencies on the LES momentum equations. This also differs from Shen et al. (2020), where the GCM large-scale pressure gradient is imposed.

The forcing fields are taken from GCM grid boxes closest to 70°N. This has more relevance for the Arctic Ocean, given the aquaplanet nature of the idealized GCM. To include synoptic-scale variability, we choose four grid points (0°, 90°, 180°, and 270° longitude) instead of using zonal-mean fields from the GCM. The results we present are averages of the 4 simulated locations, which are statistically identical. We call this average the ensemble mean.

### 2.5 Surface Forcing

To have consistent surface states, we prescribe sea ice thickness in PyCLES from GCM output, updated every 6 hours. This ensures consistent bottom boundary conditions in the GCM and LES, and it indirectly constrains the turbulent heat fluxes. Surface heat fluxes and temperatures are calculated interactively in the LES, thus slight differences are present between the LES and GCM. We have tested directly prescribing surface turbulent heat fluxes instead of sea ice thickness, which lead to unreasonable air temperatures in the LES near the surface. We find that prescribing sea ice thickness is a good compromise to obtain comparable surface conditions in the GCM and LES.

## 3 Results

### 3.1 Seasonal Cycle

The high-frequency forcing introduces a large amount of variability in the LES simulations. For better visualization, we apply a 10-day lowpass 5th order Butterworth filter to smooth the 6-hourly LES output. Figure 3 shows the seasonal cycle of the surface state and cloud condensates from the GCM-forced LES. Also shown is the insolation forcing at TOA, which corresponds well with the increase of surface temperature $T_\mathrm{s}$ from mid winter to mid spring when ice thickness reaches its maximum of 1.4 m (Figure 3a and 3b). As $T_\mathrm{s}$ reaches the melting temperature, all shortwave forcing is used to melt the sea ice, and the ice thickness declines into summer. Then $T_\mathrm{s}$ increases again above the melting temperature, but quickly decreases as insolation declines and sea ice thickens into winter. Overall, there is a good agreement between LES and GCM $T_\mathrm{s}$, with the largest difference of 5 K in winter. The variation of surface temperature is about 30 K, which is within the observed range (26–36 K) of the annual variation of monthly-mean near-surface temperatures in the Arctic (Persson, 2002).

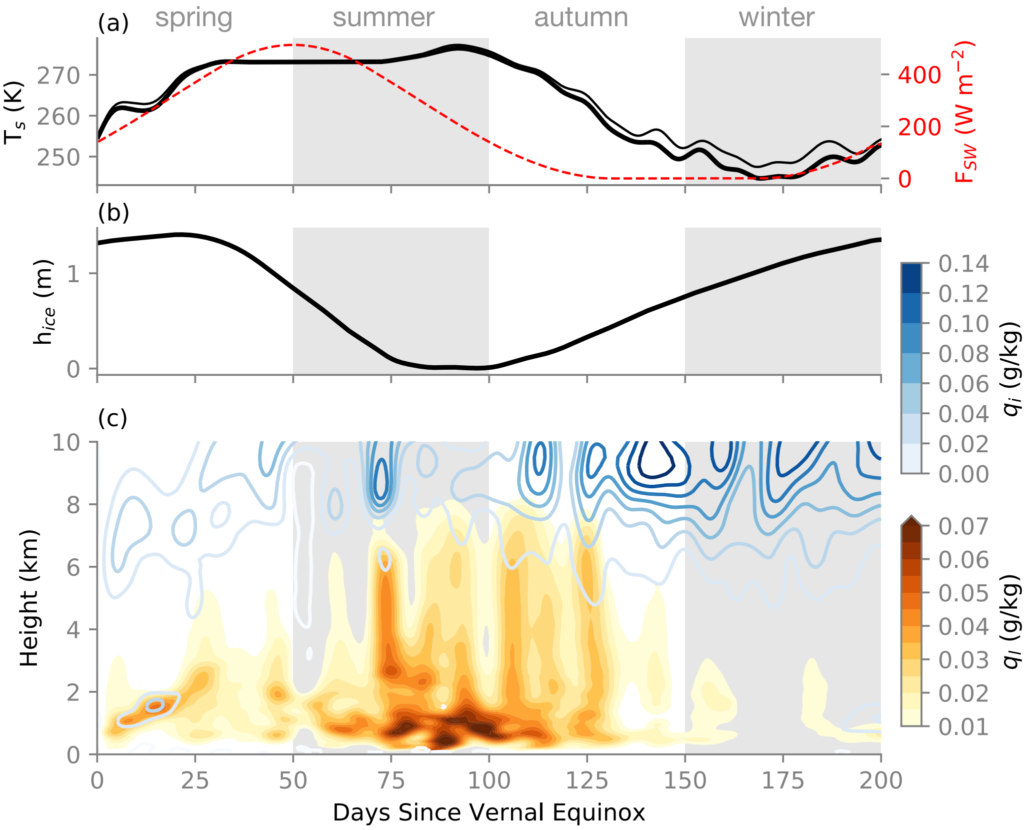


**Figure 3.** LES ensemble-mean seasonal cycle of domain-mean (a) surface temperature and TOA shortwave radiative flux, (b) sea ice thickness, and (c) cloud condensate profiles (filled colors for liquid water, contours for ice). GCM surface temperature is shown as the thin black line. Data are smoothed by a 10-day lowpass filter.

The maximum cloud liquid is found within the boundary layer during summer and autumn, when the surface temperature $T_\mathrm{s}$ is high and ice thickness $h_\mathrm{i}$ is low (Figure 3c). This is also when cloud liquid reaches the highest vertical extent at about 8 km. Cloud liquid is present throughout spring, but with lower vertical extent, and it becomes intermittent during winter. Cloud ice, on the other hand, has its maximum in winter in the upper troposphere, and it is present throughout the year. The general pattern of the seasonal cycle of clouds resembles that of the observed Arctic Ocean cloud fraction (Cesana et al., 2012): the maximum liquid cloud fraction is found in summer and early autumn, though lower liquid cloud amount persists in winter in the lower troposphere; the highest liquid cloud tops are also found during summer and early autumn, reaching 8 km.

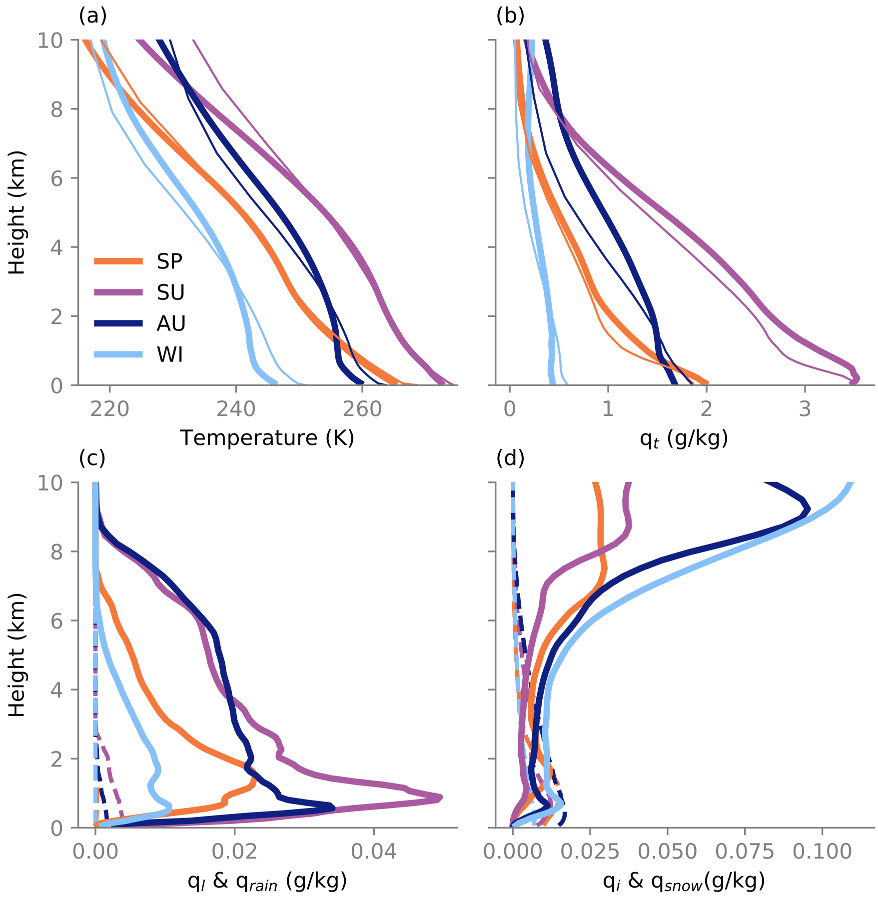


**Figure 4.** LES seasonal (50-day average) domain-mean profiles of (a) temperature, (b) total water specific humidity, (c) liquid water (solid) and rain (dashed) specific humidity, and (d) ice water (solid) and snow (dashed) specific humidity. Thin lines in (a) and (b) show the GCM values for comparison.

The polar region experiences large seasonal variations in its thermodynamic profiles, which is simulated by both the idealized GCM and the LES (Figure 4). In addition to the large differences in the temperature magnitudes across the seasons, the static stability also differs substantially (Figure 4a). Although there is no temperature inversion in the boundary layer, the lower troposphere is more stable in autumn and winter when insolation is weaker, and is more convective in spring and summer when insolation is stronger. The boundary layer is also moister in summer and spring, although in autumn the free troposphere is moister than in spring (Figure 4b).

Cloud water profiles also display large seasonal variability. Liquid water specific humidity $q_l$ peaks in the lower troposphere below 2 km throughout the year. The $q_l$ peak in summer is five times the $q_l$ peak in winter (Figure 4c). The $q_l$ peak below 1 km in summer and autumn further indicates the presence of the stratiform layers (also apparent in Figure 3c). In contrast, ice water specific humidity $q_i$ peaks in the upper troposphere, and maximizes in winter (Figure 4d). Rain is negligible, but there is a significant amount of snow in the lower troposphere, with a magnitude that is comparable to $q_l$.

Most of the clouds contain ice at higher altitudes, as seen in Figure 3c. Low clouds, on the other hand, are dominated by liquid except in winter. Ice clouds are mainly found in the upper troposphere above the liquid-containing clouds. The $q_i$ maximum is in the upper troposphere throughout the year, from 7 km in spring to 10 km in winter. Although the $q_i$ maximum is about twice the $q_l$ maximum, the ice water concentration ($q_i \rho_{\mathrm{air}}$) maximum is much lower than the liquid water concentration. The dominant precipitating species in our simulations is snow. Most snow is found in spring and autumn, and the $q_{\mathrm{snow}}$ maximum is located at the base of the liquid stratiform layer, below 2 km. This is consistent with simulations of Arctic stratocumulus. It suggests that $q_{\mathrm{snow}}$ forms mostly from autoconversion of liquid water in the middle to lower troposphere, instead of from ice water in the upper troposphere.

The seasonal cycle of condensed water paths integrated over the lower 10 km of the LES domain is shown in Figure 5. Cloud liquid water path (LWP) exhibits a seasonal cycle with a maximum of 0.25 kg m$^{-2}$ in summer and a minimum of 0.03 kg m$^{-2}$ in winter (Figure 5a). Cloud ice water path (IWP) shows a shifted seasonal cycle that peaks at 0.25 kg m$^{-2}$ in winter (Figure 5b). Intuitively, LWP is the dominant cloud condensate in summer, while IWP dominates in winter, due to the temperature dependency of the liquid fraction shown by equation (1). The snow water path is nonzero throughout the year and exceeds the rain water path.

### 3.2 Estimating Cloud Radiative Effects

Although the gray radiation scheme does not allow cloud-radiation interactions in either the GCM or the LES, one can use an offline radiative transfer model to estimate the radiative effects of the clouds in the LES. To do so, we use the Rapid Radiative Transform Model for GCMs (RRTMG) (Iacono et al., 2008). Domain-mean profiles of 6-hourly

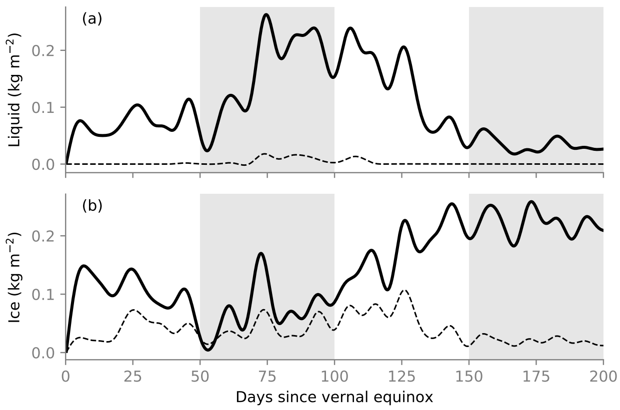


**Figure 5.** Seasonal cycle of ensemble-mean (a) liquid water path (solid) and rain water path (dashed), and (b) ice water path (solid) and snow water path (dashed). Data are smoothed by a 10-day lowpass filter.

temperature, specific humidity, pressure, density, and cloud condensates are used as input fields for RRTMG. We define the longwave and shortwave cloud radiative effects (CREs) as the difference between net all-sky fluxes and clear-sky fluxes, either at TOA or at the surface:

$$\mathrm{LWCRE} = (\mathrm{LW}^{\downarrow}_{\mathrm{all-sky}} - \mathrm{LW}^{\uparrow}_{\mathrm{all-sky}}) - (\mathrm{LW}^{\downarrow}_{\mathrm{clear}} - \mathrm{LW}^{\uparrow}_{\mathrm{clear}}), \tag{10}$$

$$\mathrm{SWCRE} = (\mathrm{SW}^{\downarrow}_{\mathrm{all-sky}} - \mathrm{SW}^{\uparrow}_{\mathrm{all-sky}}) - (\mathrm{SW}^{\downarrow}_{\mathrm{clear}} - \mathrm{SW}^{\uparrow}_{\mathrm{clear}}), \tag{11}$$

$$\mathrm{CRE} = \mathrm{LWCRE} + \mathrm{SWCRE}. \tag{12}$$

The annual-mean CRE at TOA and at the surface are summarized in Table 1, along with the observed climatological values from CERES-EBAF averaged over 70–75°N. The observed net effect of clouds at TOA is to cool the climate, dominated by SWCRE. For the LES, when both cloud liquid and ice are included in the radiative transfer calculation, the LWCRE term dominates because there is excessive cloud ice in the upper troposphere in our simulations. If we only include cloud liquid water in the calculation, the annual-mean values based on the LES are much closer to observations. Surface CRE is not as sensitive to upper-tropospheric cloud ice, since cloud liquid in the lower troposphere is already optically thick. The surface CRE based on our LES closely matches that observed. Because of the closer match with observations, we focus on the liquid CRE in our analysis here, and defer the discussion on cloud ice bias to Section 4.

**Table 1.** Ensemble-mean annual-mean cloud radiative effect at TOA and surface. For comparison, we show the CERES-EBAF 4.0 climatology averaged from 07/2005 through 06/2015.

| CRE (W m$^{-2}$) | TOA | | | SFC | | |
|---|---|---|---|---|---|---|
| | LW | SW | Net | LW | SW | Net |
| CERES-EBAF | 14 | -25 | -10 | 41 | -27 | 15 |
| Cloud liquid + ice | 41 | -33 | 7.9 | 45 | -27 | 17 |
| Cloud liquid only | 14 | -26 | -12 | 39 | -22 | 16 |

Figure 6 shows the seasonal cycle of CRE at TOA and at the surface using cloud liquid only in the calculations. The ensemble mean CRE is the average of 4 offline radiative transfer calculations from each LES simulation (as opposed to the offline calculation of the ensemble mean clouds). The seasonal cycle of TOA CRE is dominated by the seasonality in SWCRE: Clouds have a strong cooling effect during the sun-lit part of the year; during polar night, their longwave warming effect dominates, as expected (Figure 6a). The seasonal cycle of LWCRE is much more muted than SWCRE, which peaks in late summer at TOA. At the surface, the LWCRE seasonal cycle is damped compared to TOA; SWCRE variability is weaker at the surface than at TOA, but still peaks in late spring (Figure 6b). The net CRE at the surface is much higher than at TOA (16 versus $-12$ W m$^{-2}$), suggesting that polar clouds warm the surface both in observations and in our LES.

# 4 Discussion

## 4.1 Comparison to Observations

An encouraging result of our experiment is the resemblance of the simulated liquid clouds to observations. Although the model setup here is highly idealized, many processes are absent, and detailed reproduction of the seasonal cycle is not a goal, the simulated seasonal cycle of clouds and CRE still resembles that observed. This suggests that the minimal building blocks for the seasonal cycle are present in this idealized setup. For example, Cesana et al. (2012) produced the seasonal cycle of cloud fraction averaged over the Arctic Ocean (70–82°N) based on a space-borne lidar (CALIPSO-GOCCP). They found the maximum frequency of occurrence of liquid clouds near the surface from May to September, and the liquid cloud reaches is maximum vertical extent at 7.5 km alti-

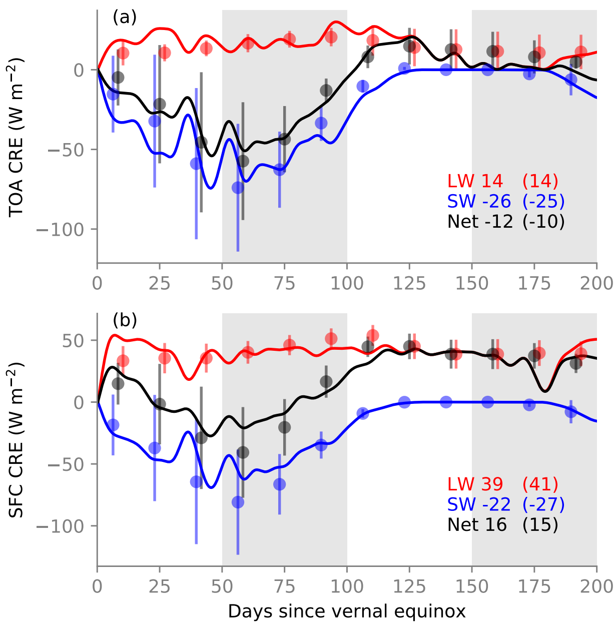


**Figure 6.** Ensemble-mean seasonal cycle of CRE due to cloud liquid only at (a) top of atmosphere and (b) surface, estimated off-line with RRTMG and domain-mean profiles. Data are smoothed by a 10-day lowpass filter. Annual mean CRE values are shown in the lower right. Dots show the observed CERES-EBAF CRE monthly climatology averaged over 70–75°N, and error bars show the spatial standard deviation for each month. Annual mean CRE values are shown in the parentheses.

tude in July. During winter, the liquid cloud fraction is lower, but liquid clouds still persist below 2 km. Ice cloud fraction is lower than liquid overall, and is zero below 4 km during June to August. The ice cloud maximum occurs at 7 km in winter, while ice cloud reaches as high as 11 km. These observations match well with the simulated seasonal cycle of clouds in our LES (Figure 3c). However, it should be borne in mind that direct comparisons between LES and observations are difficult because the spatial scales and definitions of cloud fractions are different in LES and in satellite-derived observations in Cesana et al. (2012). A more sophisticated comparison should involve satellite simulators that convert simulated thermodynamic fields to variables that are directly measured by satellites (Chepfer et al., 2008; Kay et al., 2016). Nonetheless, the similarity of the LES to observations provides evidence for the physical relevance of our experiments.

We can also compare the integrated cloud condensates with satellite observations over the Arctic Ocean north of 60°N (Figure 2 in Lenaerts et al. (2017)). The observed

LWP ranges from 0.015 to 0.125 kg m$^{-2}$, with the maximum occurring during late summer and the minimum during winter. Although the maximum ensemble-mean LWP during summer in our LES is over-estimated (0.15 kg m$^{-2}$), the timing of the maximum and minimum is consistent with the observed LWP in polar oceans (Figure 5a). Larger discrepancies are found in IWP. The observed IWP over the Arctic Ocean ranges from 0.01 to 0.11 kg m$^{-2}$. In the LES, the ensemble-mean IWP ranges from 0.07 to 0.4 kg m$^{-2}$ (Figure 5b), much higher than observed. The seasonal cycle of IWP is weak in observations, and our results show a peak in IWP during winter. The cloud ice excess in the LES may be related to our simple treatment of ice microphysics and an inefficient removal of ice particles at high altitudes. Interestingly, comprehensive climate models of the CMIP5 generation tend to underestimate IWP (Lenaerts et al., 2017).

Being aware of the biases in our simulated cloud fields, we can compare our estimated liquid CRE to observations from CERES-EBAF (Loeb et al., 2017; Kato et al., 2018). We choose all longitudes in the latitude band 70–75°N to get average observed radiative fluxes. The selected domain covers the seasonal sea ice edge, providing the relevant comparison to our idealized experiment. The monthly data from CERES-EBAF are scaled in time to match the accelerated seasonal cycle of our LES (Figure 6). The observed SWCRE shows high standard deviations during sunlit months, but the observed LWCRE shows low standard deviations in warmer months. As a result, our simulated SWCRE is generally within the observed range during the highly variable spring and early summer months. Our simulated LWCRE is too strong in spring, and TOA SWCRE is stronger in late summer/early autumn compared to CERES-EBAF. Nonetheless, our simulated annual-mean TOA LWCRE and SWCRE based on cloud liquid alone agree well with observations.

### 4.2 Forcing and Clouds

What determines the seasonal cycle of Arctic clouds? Radiation is the zeroth-order driver for any seasonal variability in temperatures in the Arctic. Moisture, on the other hand, comes from either large-scale advection or surface evaporation. Condensation depends on both temperature and moisture forcing.

The external non-radiative forcing for clouds in our LES includes two components: large-scale advection and surface fluxes. These two are not independent of one another

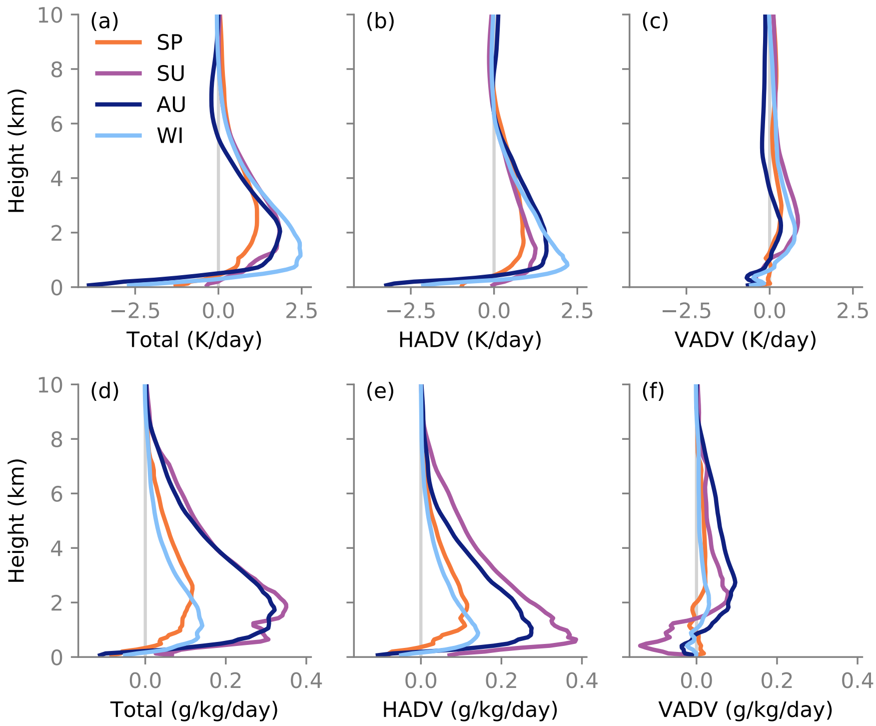


**Figure 7.** Seasonal average profiles of large-scale forcing of (a) total temperature advection, (b) horizontal temperature advection, (c) vertical temperature advection, (d) total specific humidity advection, (e) horizontal specific humidity advection, and (f) vertical specific humidity advection.Horizontal advection (HADV) is taken directly from the GCM, while vertical advection (VADV) is a hybrid of GCM and LES fields.

in the real climate system. Large-scale advection is more important at high latitudes than at lower latitudes, because of the large atmospheric heat transport that balances the net negative radiative forcing at TOA. Large-scale advection brings heat and moisture into the high latitudes year-round (Figure 7a and 7d). For both temperature and specific humidity advection, the horizontal advection terms dominate (Figure 7b and 7e). Temperature advection is the strongest in winter, when the pole-to-equator temperature gradient is the strongest. Summer temperature advection is weak, but it is associated with the largest moisture advection. On the other hand, moisture advection is weak in winter and spring, contributing to a polar atmosphere that is cold and dry. The moisture advection seasonal cycle is consistent with the observed horizontal moisture advection north of 70°N, but our simulations have peak values in summer that are twice the reanalysis values (Serreze et al., 2007; Newman et al., 2012). At the surface, evaporation

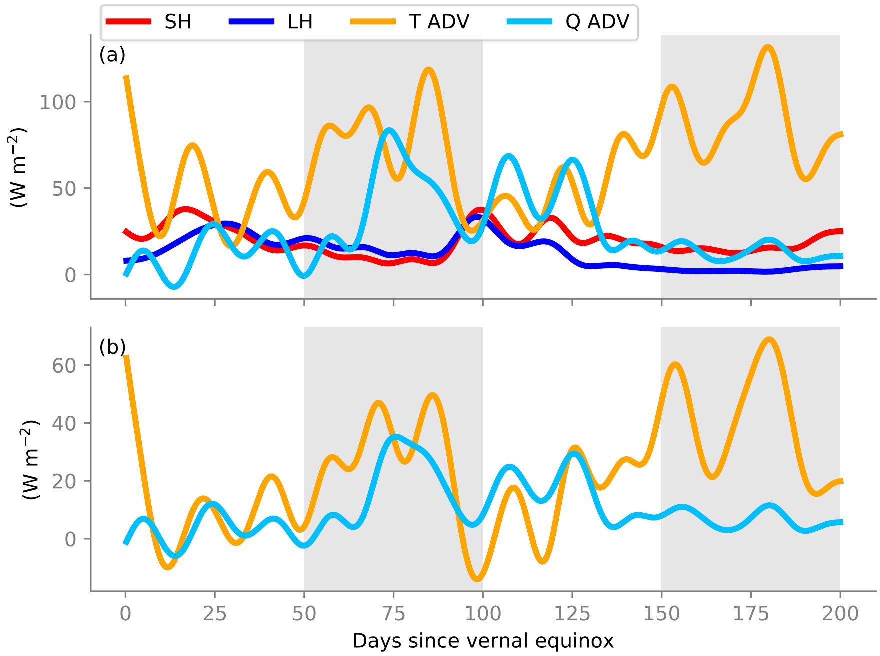


**Figure 8.** (a) Seasonal cycle of vertically integrated total temperature and specific humidity advection (converted to dry and latent energy fluxes), as well as sensible and latent heat fluxes at the surface. (b) Seasonal cycle of total temperature and moisture advection integrated over the bottom 2 km. Data are smoothed by a 10-day lowpass filter.

is limited in winter but provides a significant source of lower-tropospheric water vapor during summer and early autumn.

Figure 8a shows the seasonal cycle of the vertically integrated large-scale forcing tendencies (with the moisture flux convergence expressed as a latent heat flux convergence), along with turbulent fluxes at the surface. There is significant synoptic variability in the large-scale advection terms from the GCM; here we focus on the overall budget and have smoothed all fields with a 10-day lowpass filter.

For the entire LES domain and throughout the year, large-scale temperature advection is stronger than the surface sensible heat flux. However, if we focus on the lowest 2 km (Figure 8b), the surface sensible heat flux is of comparable magnitude to the large-scale temperature advection in the boundary layer. Moisture advection is strongest in summer and autumn, both in the boundary layer and in the entire troposphere. In spring when moisture advection reaches its minimum, surface latent heat flux becomes the dominant moisture source. In winter, large-scale moisture advection contributes more to the moisture budget than the surface latent heat flux.

The concurrence between the moisture advection peak and cloud liquid maximum (Figure 8a and 5a) points to the dominant role that large-scale moisture advection plays in governing the seasonal cycle of cloud liquid in the polar region. In summer, air temperatures continue to rise and so does the saturation specific humidity. A moisture source is needed for condensation to occur during this period, and in our case the source comes from large-scale advection of water vapor. Air temperatures begin to decrease at the end of summer, which lowers the saturation specific humidity. Cloud condensates form in autumn due to both cooling and a continued supply of water vapor from large-scale advection. In winter, the peak in large-scale temperature advection warms the troposphere, making it harder to form cloud condensates.

Beesley and Moritz (1999) tested the sensitivity to large-scale advection of moisture by swapping summer and winter moisture advection in a single-column model. They found little changes in the simulated cloud fraction. However, both liquid and ice water paths were doubled in winter when summer moisture advection is applied (roughly doubling the winter moisture advection). Their insensitivity of cloud fraction to moisture advection may be due to biases in the mean state, such as the lack of high-frequency variability in the forcing. In future work, we plan to analyze how large-scale advection from reanalysis and comprehensive GCMs affects LES cloud cover, to better assess the influence of forcing magnitude and frequency.

### 4.3 Limitations

Although the idealized GCM has been shown to capture many large-scale features of the atmospheric circulation, not all aspects are accurately simulated. Known biases such as jet stream biases and in the storm track response to warming exist (e.g., Tan et al., 2019). Furthermore, the GCM used in the study has a positive relative humidity bias in the polar regions. According to reanalysis, the climatological relative humidity in the free troposphere is between 65% and 70% at 70°N. In the idealized GCM, the relative humidity is at least 10% higher. This leads to a moist bias in the LES, manifested in the excessive IWP (Figure 5b) and high ice water specific humidity in the upper troposphere (Figure 3c). The lack of continents may partly explain the over-estimated summer moisture advection into the polar region, as mentioned in section 4.2. We will address these issues in future revisions of the experimental design to improve our understanding of polar cloud dynamics.

Our use of a one-moment bulk microphysics scheme can be limiting in reproducing the observed cloud seasonal cycle, and especially the ice phase. IWP in our LES is about 4 times higher than what is seen in observations over the Arctic Ocean (Lenaerts et al., 2017). We tested the sensitivity of our results to the formulation of liquid fraction (Figure 1) by using the observationally derived formula in Hu et al. (2010), with higher liquid to ice ratio above 246 K, vice versa below 246 K, and the largest modification in liquid fractions at temperatures around 240 K (Figure S1). With this modification in the LES, we found the largest modification in $q_l$ at temperatures above 240 K because of the exponential nature of the Clausius-Clapeyron relation. As a result, LWP is higher in summer to autumn and lower in winter in the simulation with Hu et al. (2010) liquid fraction (Figure S2). Its effect on liquid CRE is strongest in winter, because there is a cancellation in LW and SW during sunlit seasons. The lowered LWP in winter due to Hu et al. (2010) liquid fraction leads to a slight reduction of LWCRE, which dominates the net CRE change of -2.4 W m$^2$ in the annual mean (Figure S3).

The lack of water vapor and cloud feedbacks in our modeling framework becomes a major drawback when it comes to representing details of cloud structures and coupling between radiation and dynamics. For example, cloud-top radiative cooling imposes a dominant forcing to the dynamics of stratocumulus (Bretherton et al., 1999). Without it, the turbulence in the boundary layer is unlikely to be strong enough to produce a well-mixed layer and an inversion above the cloud tops. Lack of this radiation-dynamics coupling explains the structural differences between our simulated clouds and observed Arctic clouds. However, our GCM-forcing framework provides a clean setup to study the role large-scale advection plays in controlling the seasonal cycle of cloud liquid. In a follow-up paper, we will use the same framework to explore the response of polar clouds to climate warming.

## 5 Conclusions

We adopted an idealized framework in which large eddy simulations are driven by large-scale forcing from a GCM in a high-latitude setting. Our approach encapsulates components of first-order importance in the polar regions, such as large-scale advection of heat and moisture, sea ice, and a simple representation of mixed-phase microphysics. Water vapor and cloud feedbacks are not represented in the gray radiative transfer schemes in both the GCM and the LES.

The seasonal cycle of simulated polar clouds resembles observations qualitatively. In particular, maximum cloud liquid is found below 2 km in summer and autumn, and it reaches minimum in winter. Cloud ice is found mostly in the upper troposphere. The condensed water path is dominated by ice, which is overestimated compared to observations. LWP, on the other hand, agrees better with satellite-derived values over the Arctic Ocean. Offline radiative transfer calculations of liquid cloud radiative effects also show encouraging agreement with CERES-EBAF: the net liquid cloud radiative effect is to cool the LES domain, but to warm the surface.

Analysis of the forcing budget points to the dominant role that large-scale advection of moisture plays in controlling the seasonal cycle of cloud liquid. In the boundary layer, surface evaporation is of comparable magnitude to large-scale moisture advection. The peak of large-scale temperature advection occurs in winter, when the pole-to-equator temperature gradient is greatest. This warms the troposphere and reduces cloud condensates.

Our idealized framework provides an opportunity to study mechanisms of cloud-climate feedbacks in the complicated polar climate system. In a follow-on paper, we will look at the polar cloud response to climate warming caused by increased longwave optical thickness of the atmosphere. We will also analyze how changes in large-scale advection with warming affect the simulated cloud amount, to pave the road for future studies with more realistic large-scale forcing.

## Acknowledgments

X.Z. is supported by an Advanced Study Program postdoctoral fellowship from the National Center for Atmospheric Research. Part of this material is based upon work supported by the National Center for Atmospheric Research, which is a major facility sponsored by the National Science Foundation under Cooperative Agreement No. 1852977. Part of this research was supported by the generosity of Eric and Wendy Schmidt by recommendation of the Schmidt Futures program, by Mountain Philanthropies, and by the

National Science Foundation (NSF grant AGS-1835860). Part of this research was carried out at the Jet Propulsion Laboratory, California Institute of Technology, under a contract with the National Aeronautics and Space Administration. The simulations were performed on Caltech's High Performing Cluster, which is partially supported by a grant from the Gordon and Betty Moore Foundation. The GCM and LES codes are available online at http://climate-dynamics.org/software. GCM forcing and LES output files are available online at https://data.caltech.edu/records/1429.

## References

Baek, E.-H., Kim, J.-H., Park, S., Kim, B.-M., & Jeong, J.-H. (2019, April). Impact of poleward heat and moisture transports on Arctic clouds and climate simulation. *Atmospheric Chemistry and Physics Discussions*, 1–19. doi: https://doi.org/10.5194/acp-2019-199

Beesley, J. A., & Moritz, R. E. (1999). Toward an Explanation of the Annual Cycle of Cloudiness over the Arctic Ocean. *Journal of Climate*, *12*, 395–415. doi: 10.1175/1520-0442(1999)012⟨0395:TAEOTA⟩2.0.CO;2

Bintanja, R., & van der Linden, E. C. (2013, December). The changing seasonal climate in the Arctic. *Scientific Reports*, *3*(1). doi: 10.1038/srep01556

Bretherton, C. S., Macvean, M. K., Bechtold, P., Chlond, A., Cotton, W. R., Cuxart, J., … Wyant, M. C. (1999). An intercomparison of radiatively driven entrainment and turbulence in a smoke cloud, as simulated by different numerical models. *Quarterly Journal of the Royal Meteorological Society*, *125*(554), 391–423. doi: 10.1002/qj.49712555402

Brient, F., Schneider, T., Tan, Z., Bony, S., Qu, X., & Hall, A. (2016). Shallowness of tropical low clouds as a predictor of climate models response to warming. *Climate Dynamics*, *47*, 433–449. doi: 10.1007/s00382-015-2846-0

Cesana, G., Kay, J. E., Chepfer, H., English, J. M., & de Boer, G. (2012). Ubiquitous low-level liquid-containing Arctic clouds: New observations and climate model constraints from CALIPSO-GOCCP. *Geophysical Research Letters*, *39*. doi: 10.1029/2012GL053385

Chepfer, H., Bony, S., Winker, D., Chiriaco, M., Dufresne, J.-L., & Sze, G. (2008). Use of CALIPSO lidar observations to evaluate the cloudiness simulated by a climate model. *Geophysical Research Letters*, *35*. doi: 10.1029/2008GL034207

Dal Gesso, S., & Neggers, R. A. J. (2018, February). Can We Use Single-Column Models for Understanding the Boundary Layer Cloud-Climate Feedback? *Journal of Advances in Modeling Earth Systems*, *10*(2), 245–261. doi: 10.1002/2017MS001113

Eisenman, I. (2007). Arctic catastrophes in an idealized sea ice model. In *2006 program of studies: Ice (geophysical fluid dynamics program)* (p. 133-161). Woods Hole Oceanog. Inst. Tech. Rept. 2007-02. (http://www.whoi.edu/page.do?pid=12938)

Eisenman, I., & Wettlaufer, J. S. (2009, January). Nonlinear threshold behavior during the loss of Arctic sea ice. *Proceedings of the National Academy of Sciences*, *106*(1), 28–32. doi: 10.1073/pnas.0806887106

Frierson, D. M. W., Held, I. M., & Zurita-Gotor, P. (2006). A gray-radiation aquaplanet moist GCM. Part I: Static stability and eddy scale. *Journal of the Atmospheric Sciences*, *63*, 2548–2566. doi: 10.1175/JAS3753.1

Frierson, D. M. W., Held, I. M., & Zurita-Gotor, P. (2007). A gray-radiation aquaplanet moist GCM. Part II: Energy rransports in altered climates. *Journal of the Atmospheric Sciences*, *64*, 1680–1693. doi: 10.1175/JAS3913.1

Grabowski, W. W. (1998). Toward cloud resolving modeling of large-scale tropical circulations: A simple cloud microphysics parameterization. *Journal of the Atmospheric Sciences*, *55*, 3283-3298.

Graversen, R. G., & Wang, M. (2009). Polar amplification in a coupled climate model with locked albedo. *Climate Dynamics*, *33*(5), 629–643.

Holland, M. M., & Bitz, C. M. (2003). Polar amplification of climate change in coupled models. *Climate Dynamics*, *21*, 221–232. doi: 10.1007/s00382-003-0332-6

Hu, Y., Rodier, S., Xu, K.-m., Sun, W., Huang, J., Lin, B., … Josset, D. (2010). Occurrence, liquid water content, and fraction of supercooled water clouds from combined CALIOP/IIR/MODIS measurements. *Journal of Geophysical Research*, *115*. (D00H34) doi: 10.1029/2009JD012384

Iacono, M. J., Delamere, J. S., Mlawer, E. J., Shephard, M. W., Clough, S. A., & Collins, W. D. (2008). Radiative forcing by long-lived greenhouse gases: Calculations with the AER radiative transfer models. *Journal of Geophysical Research*, *113*. (D13103) doi: 10.1029/2008JD009944

Karlsson, J., & Svensson, G. (2013). Consequences of poor representation of Arctic sea-ice albedo and cloud-radiation interactions in the CMIP5 model ensemble. *Geophysical Research Letters*, *40*, 4374–4379. doi: 10.1002/grl.50768

Kato, S., Rose, F. G., Rutan, D. A., Thorsen, T. J., Loeb, N. G., Doelling, D. R., … Ham, S.-H. (2018, March). Surface Irradiances of Edition 4.0 Clouds and the Earths Radiant Energy System (CERES) Energy Balanced and Filled (EBAF) Data Product. *Journal of Climate*, *31*, 4501–4527. doi: 10.1175/JCLI-D-17-0523.1

Kaul, C. M., Teixeira, J., & Suzuki, K. (2015). Sensitivities in large-eddy simulations of mixed-phase Arctic stratocumulus clouds using a simple microphysics approach. *Monthly Weather Review*, *143*, 4393-4421. doi: 10.1175/MWR-D-14-00319.1

Kay, J. E., L'Ecuyer, T., Chepfer, H., Loeb, N., Morrison, A., & Cesana, G. (2016). Recent advances in Arctic cloud and climate research. *Current Climate Change Reports*, *2*(4), 159–169.

Klein, S. A., McCoy, R. B., Morrison, H., Ackerman, A. S., Avramov, A., Boer, G. d., … Zhang, G. (2009). Intercomparison of model simulations of mixed-phase clouds observed during the ARM Mixed-Phase Arctic Cloud Experiment. I: single-layer cloud. *Quarterly Journal of the Royal Meteorological Society*, *135*, 979–1002. doi: 10.1002/qj.416

Kretzschmar, J., Salzmann, M., Mlmenstdt, J., & Quaas, J. (2019, August). Arctic clouds in ECHAM6 and their sensitivity to cloud microphysics and surface fluxes. *Atmospheric Chemistry and Physics*, *19*(16), 10571–10589. doi: https://doi.org/10.5194/acp-19-10571-2019

Laîné, A., Yoshimori, M., & Abe-Ouchi, A. (2016, May). Surface Arctic Amplification Factors in CMIP5 Models: Land and Oceanic Surfaces and Seasonality. *Journal of Climate*, *29*(9), 3297–3316. doi: 10.1175/JCLI-D-15-0497.1

Lenaerts, J. T. M., VanTricht, K., Lhermitte, S., & L'Ecuyer, T. S. (2017). Polar clouds and radiation in satellite observations, reanalyses, and climate models. *Geophysical Research Letters*, *44*, 3355–3364. doi: 10.1002/2016GL072242

Loeb, N. G., Doelling, D. R., Wang, H., Su, W., Nguyen, C., Corbett, J. G., … Kato, S. (2017, November). Clouds and the Earths Radiant Energy System (CERES) Energy Balanced and Filled (EBAF) Top-of-Atmosphere

(TOA) Edition-4.0 Data Product. *Journal of Climate*, *31*(2), 895–918. doi: 10.1175/JCLI-D-17-0208.1

Morrison, H., Zuidema, P., Ackerman, A. S., Avramov, A., de Boer, G., Fan, J., … Shipway, B. (2011, February). Intercomparison of cloud model simulations of Arctic mixed-phase boundary layer clouds observed during SHEBA/FIRE-ACE. *Journal of Advances in Modeling Earth Systems*, *3*(2). doi: 10.1029/2011MS000066

Newman, M., Kiladis, G. N., Weickmann, K. M., Ralph, F. M., & Sardeshmukh, P. D. (2012, May). Relative contributions of synoptic and low-frequency eddies to time-mean atmospheric moisture transport, including the role of atmospheric rivers. *Journal of Climate*, *25*(21), 7341–7361. (Publisher: American Meteorological Society) doi: 10.1175/JCLI-D-11-00665.1

O'Gorman, P. A., & Schneider, T. (2008). The hydrological cycle over a wide range of climates simulated with an idealized GCM. *Journal of Climate*, *21*, 3815–3832. doi: 10.1175/2007JCLI2065.1

Ovchinnikov, M., Ackerman, A. S., Avramov, A., Cheng, A., Fan, J., Fridlind, A. M., … Sulia, K. (2014). Intercomparison of large-eddy simulations of Arctic mixed-phase clouds: Importance of ice size distribution assumptions. *Journal of Advances in Modeling Earth Systems*, *6*, 223–248. doi: 10.1002/2013MS000282

Persson, P. O. G. (2002). Measurements near the atmospheric surface flux group tower at SHEBA: Near-surface conditions and surface energy budget. *Journal of Geophysical Research*, *107*. doi: 10.1029/2000JC000705

Pithan, F., & Mauritsen, T. (2014). Arctic amplification dominated by temperature feedbacks in contemporary climate models. *Nature Geosciences*, *7*(3), 181–184.

Pressel, K. G., Kaul, C. M., Schneider, T., Tan, Z., & Mishra, S. (2015). Large-eddy simulation in an anelastic framework with closed water and entropy balances. *Journal of Advances in Modeling Earth Systems*. doi: 10.1002/2015MS000496

Pressel, K. G., Mishra, S., Schneider, T., Kaul, C. M., & Tan, Z. (2017). Numerics and subgrid-scale modeling in large eddy simulations of stratocumulus clouds. *Journal of Advances in Modeling Earth Systems*. doi: 10.1002/2016MS000778

Savre, J., Ekman, A. M. L., Svensson, G., & Tjernstrm, M. (2015). Large-eddy simulations of an Arctic mixed-phase stratiform cloud observed during ISDAC: sensitivity to moisture aloft, surface fluxes and large-scale forcing. *Quarterly Journal of the Royal Meteorological Society*, *141*, 1177–1190. doi: 10.1002/qj.2425

Schneider, T., Kaul, C. M., & Pressel, K. G. (2019). Possible climate transitions from breakup of stratocumulus decks under greenhouse warming. *Nature Geosci.*, *12*, 163–167.

Schneider, T., Teixeira, J., Bretherton, C. S., Brient, F., Pressel, K. G., Schar, C., & Siebesma, A. P. (2017). Climate goals and computing the future of clouds. *Nature Clim. Change*, *7*, 3–5.

Screen, J. A., Deser, C., & Simmonds, I. (2012). Local and remote controls on observed Arctic warming. *Geophysical Research Letters*, *39*. (L10709) doi: 10.1029/2012GL051598

Sekhon, R. S., & Srivastava, R. C. (1970). Snow Size Spectra and Radar Reflectivity. *Journal of the Atmospheric Sciences*, *27*, 299–307. doi: 10.1175/1520-0469(1970)027⟨0299:SSSARR⟩2.0.CO;2

Semtner, A. J. (1976). A Model for the Thermodynamic Growth of Sea Ice in Numerical Investigations of Climate. *Journal of Physical Oceanography*, *6*, 379–389. doi: 10.1175/1520-0485(1976)006⟨0379:AMFTTG⟩2.0.CO;2

Serreze, M. C., Barrett, A. P., Slater, A. G., Steele, M., Zhang, J., & Trenberth, K. E. (2007, June). The large-scale energy budget of the Arctic. *Journal of Geophysical Research*, *112*(D11). doi: 10.1029/2006JD008230

Serreze, M. C., Barrett, A. P., Stroeve, J. C., Kindig, D. N., & Holland, M. M. (2009). The emergence of surface-based Arctic amplification. *The Cryosphere*, *3*, 11–19. doi: 10.5194/tc-3-11-2009

Shen, Z., Pressel, K. G., Tan, Z., & Schneider, T. (2020). Statistically steady state large-eddy simulations forced by an idealized GCM: 1. Forcing framework and simulation characteristics. *Journal of Advances in Modeling Earth Systems*, *12*. doi: 10.1029/2019MS001814

Shupe, M. D., & Intrieri, J. M. (2004). Cloud radiative forcing of the Arctic surface: The influence of cloud properties, surface albedo, and solar zenith angle. *Journal of Climate*, *17*, 616–628. doi: 10.1175/1520-0442(2004)017⟨0616:CRFOTA⟩2.0.CO;2

Tan, Z., Lachmy, O., & Shaw, T. A. (2019). The sensitivity of the jet stream response to climate change to radiative assumptions. *Journal of Advances in Modeling Earth Systems*, *11*(4), 934–956. doi: 10.1029/2018MS001492

Tan, Z., Schneider, T., Teixeira, J., & Pressel, K. G. (2016). Large-eddy simulation of subtropical cloud-topped boundary layers: 1. A forcing framework with closed surface energy balance. *Journal of Advances in Modeling Earth Systems*. doi: 10.1002/2016MS000655

Tan, Z., Schneider, T., Teixeira, J., & Pressel, K. G. (2017). Large-eddy simulation of subtropical cloud-topped boundary layers: 2. Cloud response to climate change. *Journal of Advances in Modeling Earth Systems*. doi: 10.1002/2016MS000804

Taylor, P. C., Boeke, R. C., Li, Y., & Thompson, D. W. J. (2019, July). Arctic cloud annual cycle biases in climate models. *Atmospheric Chemistry and Physics*, *19*(13), 8759–8782. doi: 10.5194/acp-19-8759-2019

Vavrus, S. (2004, February). The Impact of Cloud Feedbacks on Arctic Climate under Greenhouse Forcing*. *Journal of Climate*, *17*(3), 603–615. doi: 10.1175/1520-0442(2004)017⟨0603:TIOCFO⟩2.0.CO;2

Yoshimori, M., Abe-Ouchi, A., Watanabe, M., Oka, A., & Ogura, T. (2014, August). Robust seasonality of Arctic warming processes in two Different versions of the MIROC GCM. *Journal of Climate*, *27*(16), 6358–6375. doi: 10.1175/JCLI-D-14-00086.1